Experimental Thermal and Fluid Science 35 (2011) 896–909

Contents lists available at ScienceDirect

Experimental Thermal and Fluid Science

journal homepage: www.elsevier.com/locate/etfs

# Free-surface fluctuations and turbulence in hydraulic jumps

Yann Chachereau, Hubert Chanson *

*The University of Queensland, School of Civil Engineering, Brisbane QLD 4072, Australia*

ARTICLE INFO

*Article history:*
Received 30 November 2010
Received in revised form 19 January 2011
Accepted 19 January 2011
Available online 16 February 2011

*Keywords:*
Hydraulic jumps
Free-surface fluctuations
Turbulence properties
Time and length scales

ABSTRACT

A hydraulic jump is the highly turbulent transition between a high-velocity impinging flow and a turbulent roller. The jump flow is characterised by some substantial air bubble entrainment, spray and splashing. In the present study, the free-surface fluctuations and air–water properties of the hydraulic jump roller were investigated physically for relatively small Froude numbers ($2.4 < Fr_1 < 5.1$) and relatively large Reynolds numbers ($6.6 \times 10^4 < Re < 1.3 \times 10^5$). The shape of the mean free surface profile was well defined, and the time-averaged free-surface elevation corresponded to the upper free-surface, with the quantitative values being close to the equivalent clear-water depth. The turbulent fluctuation profiles exhibited a maximum in the first part of the hydraulic jump roller. The free-surface fluctuations presented some characteristic frequencies between 1.4 and 4 Hz. Some simultaneous free-surface measurements at a series of two closely located points yielded the free-surface length and time scales of free-surface fluctuations in terms of both longitudinal and transverse directions. The length scale data seemed to depend upon the inflow Froude number, while the time scale data showed no definite trend. Some simultaneous measurements of instantaneous void fraction and free-surface fluctuations exhibited different features depending upon the phase-detection probe sensor location in the different regions of the roller.



## 1. Introduction

A hydraulic jump is the highly turbulent transition from a high-velocity flow to a slower flow motion. The jump toe is a discontinuity between the impinging flow and the roller (Fig. 1). The hydraulic jump flow is characterised by some substantial air bubble entrainment, spray and splashing. In the turbulent flow region called the roller, two distinctive air–water regions are seen: the air–water mixing layer and the upper free-surface layer. In the mixing layer, there is a transfer of momentum from the high-velocity jet flow to the recirculation region above, as well as by an advective transport of the entrained air bubbles. Considering a hydraulic jump in a horizontal rectangular channel, the application of the equations of conservation of mass and momentum in their integral form yields a series of relationship between the flow properties downstream of and upstream of the jump:

$$\frac{d_2}{d_1} = \frac{1}{2}\left(\sqrt{1+8Fr_{12}} - 1\right) \quad (1)$$

$$\frac{Fr_2}{Fr_1} = \frac{2^{3/2}}{\left(\sqrt{1+8Fr_{12}} - 1\right)^{3/2}} \quad (2)$$

where $d_1$ and $d_2$ are respectively the upstream and downstream flow depths, $Fr_1$ and $Fr_2$ are the upstream and downstream Froude numbers respectively, the Froude number is defined as $Fr = V/\sqrt{gd}$, $V$ is the flow velocity and $g$ is the gravity acceleration. Eq. (1) is called sometimes the Bélanger equation, first developed by Jean-Baptiste Bélanger in 1838 [1,6].

The hydraulic jumps are commonly encountered in hydraulic structures and stilling basins, storm waterways, water treatment plants and chemical processing plants. A classical example is the circular hydraulic jump in a sink. Fig. 1A shows a hydraulic jump in an irrigation channel. The discharge per unit width was about 0.5 $m^3/s$ corresponding to a Reynolds number of $1 \times 10^5$. Fig. 1B presents a hydraulic jump in the inlet structure and mixer of a water treatment plant.

The turbulent free-surface properties above a hydraulic jump were rarely investigated, but for Mouaze et al. [14] and Murzyn and Chanson [15]. The former study was based upon wire gage sensors commonly used for nonbreaking periodic waves. The latter was conducted with non-intrusive acoustic displacement sensors with a faster dynamic response.

In the present study, the free-surface fluctuations and air–water flow properties were investigated in hydraulic jumps with relatively small Froude numbers and large Reynolds numbers. Both non-intrusive acoustic displacement sensors and intrusive phase-detection probes were used. It is the aim of this work to characterise the unsteady free surface motion and the air–water flow

* Corresponding author. Tel.: +61 7 33 65 35 16; fax: +61 7 33 65 45 99.
*E-mail address:* h.chanson@uq.edu.au (H. Chanson).
*URL:* http://www.uq.edu.au/~e2hchans/ (H. Chanson).

0894-1777/$ - see front matter © 2011 Elsevier Inc. All rights reserved.
doi:10.1016/j.expthermflusci.2011.01.009

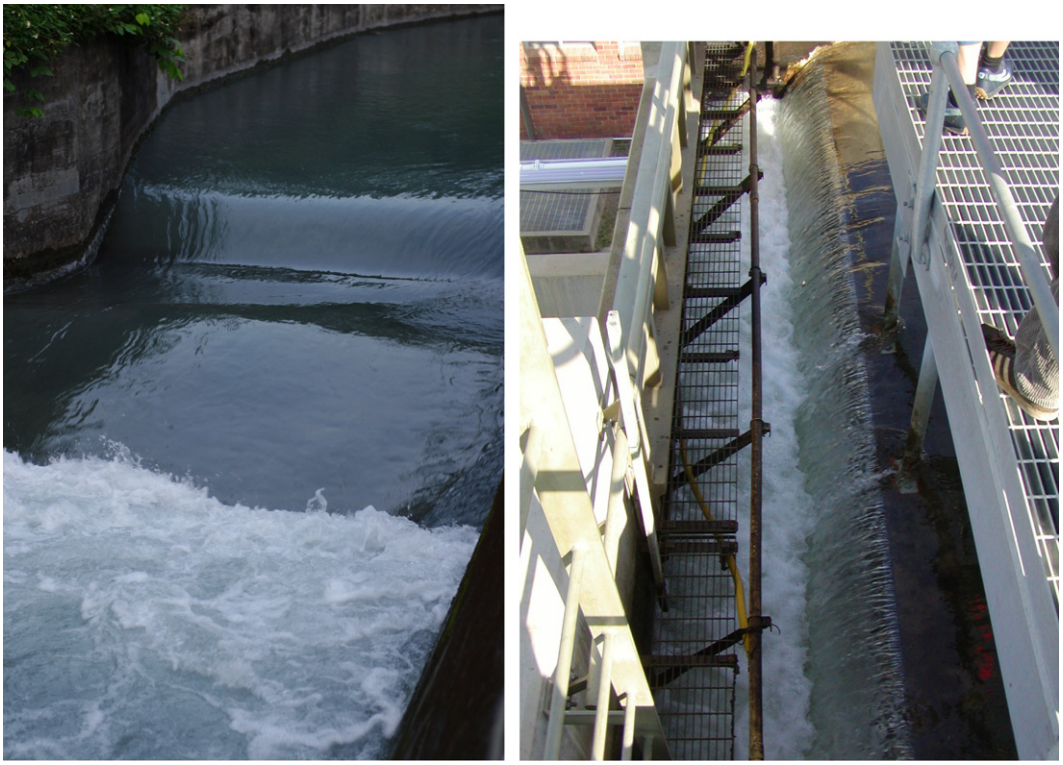

(A, Left) Hydraulic jump in an irrigation channel on 10 November 2010 in Hualien County (Taiwan) - Flow from top right to bottom left (Shutter speed: 1/100 s)

(B, right) Hydraulic jump in the Molendinar water processing plant (Gold Coast, Australia) on 4 September 2002

**Fig. 1.** Photographs of prototype hydraulic jumps.

properties in hydraulic jumps for a broad range of relatively small Froude numbers ($2.4 < Fr_1 < 5.1$).

## 2. Experimental facility and instrumentation

### 2.1. Experimental set-up and instrumentation

The experiments were performed in a 3.2 m long, 0.5 m wide horizontal rectangular channel (Fig. 2). The glass sidewall height was 0.45 m and the channel bed was made of PVC. The inflow conditions were controlled by a vertical gate with a semi-circular shape ($\varnothing = 0.3$ m), and the upstream gate opening was fixed during all experiments at $h = 0.036$ m. This channel was previously used with different flow conditions by Chanson [5], Kucukali and Chanson [11] and Murzyn and Chanson [15].

The water discharge was measured with a Venturi metre located in the supply line which was calibrated on-site. The discharge measurement was accurate within ±2%. The clear-water flow depths were measured using rail mounted point gages with a 0.2 mm accuracy. The pressure and velocity measurements in steady supercritical flows were performed with a Prandtl–Pitot tube. Its performances were compared with a British Standards design within 1% in wind tunnel tests for Reynolds numbers ranging from $1 \times 10^5$ to $9 \times 10^5$. The Prandtl–Pitot tube had an external diameter $\varnothing = 3.02$ mm, the total head was measured through a 1 mm hole at the tip, and the distance between the tip of the probe and the lateral pressure points ($\varnothing = 0.5$ mm) was 9 mm.

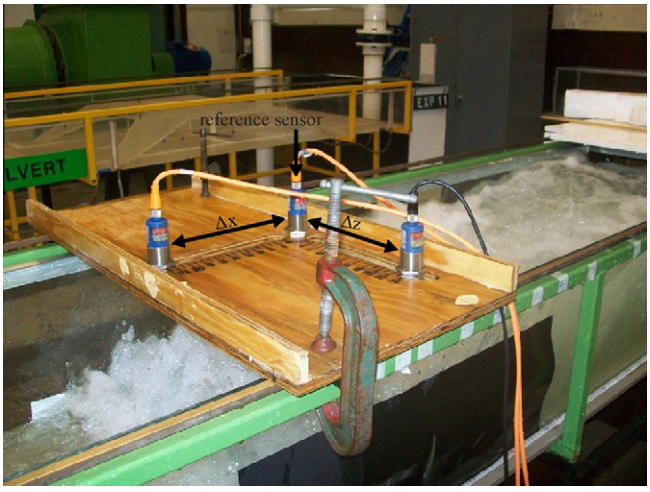


**Fig. 2.** Experimental setup with three acoustic displacement metres and definition of the longitudinal and transverse separation distances $\Delta x$ and $\Delta z$ – flow from left to right: $d_1 = 39.5$ mm, $x_1 = 1.50$ m, $Fr_1 = 5.1$, Re = $1.3 \times 10^5$.

Further details on the experimental facility, instrumentation and data sets were reported in Chachereau and Chanson [3].

#### 2.1.1. Free-surface measurements using acoustic displacement metres

The instantaneous free-surface elevations were measured using several ultrasonic displacement metres Microsonic™ located along

**Table 1**
Longitudinal positions of the acoustic displacement sensors (Jump toe location: $x_1$ = 1.50 m).

| Sensor name | $S_0$ | $S_1$ | $S_2$ | $S_3$ | $S_4$ | $S_5$ | $S_6$ |
|---|---|---|---|---|---|---|---|
| $x$ (m) | 1.35 | 1.595 | 1.74 | 1.94 | 2.19 | 2.43 | 2.67 |
| $x - x_1$ (m) | −0.15 | +0.095 | +0.24 | +0.44 | +0.69 | +0.93 | +1.17 |
| Sensor type | Mic + 35 | Mic + 25 | Mic + 25 | Mic + 25 | Mic + 25 | Mic + 25 | Mic + 25 |

**Table 2**
Developing boundary layer properties upstream of the hydraulic jump (Present study).

| $Q$ ($m^3$/s) | $h$ (m) | $d_1$ (m) | $Fr_1$ | Re | $x/d_1$ | $\delta/d_1$ | $\delta_1/d_1$ | $\delta_2/d_1$ | $\delta_3/d_1$ | $V_{max}$ (m/s) |
|---|---|---|---|---|---|---|---|---|---|---|
| 0.0446 | 0.036 | 0.044 | 3.1 | $8.9 \times 10^4$ | 9.1 | 0.151 | 0.0096 | 0.0085 | 0.0162 | 2.6 |
| | | | | | 17 | 0.138 | 0.0058 | 0.0055 | 0.0106 | 2.59 |
| | | | | | 21.1 | 0.114 | 0.0059 | 0.0054 | 0.0103 | 2.57 |
| | | | | | 24.3 | 0.12 | 0.0076 | 0.0068 | 0.0129 | 2.55 |
| | | | | | 25 | 0.125 | 0.0088 | 0.0078 | 0.0147 | 2.55 |
| | | | | | 31.8 | 0.117 | 0.0077 | 0.0068 | 0.0129 | 2.53 |
| 0.049 | 0.036 | 0.0405 | 3.8 | $9.8 \times 10^4$ | 9.9 | 0.129 | 0.0088 | 0.0078 | 0.0147 | 2.86 |
| | | | | | 18.5 | 0.173 | 0.0104 | 0.0094 | 0.0179 | 2.84 |
| | | | | | 27.2 | 0.158 | 0.0097 | 0.0088 | 0.0169 | 2.82 |
| | | | | | 34.6 | 0.135 | 0.0104 | 0.0091 | 0.0172 | 2.8 |
| 0.0545 | 0.036 | 0.0395 | 4.4 | $1.1 \times 10^5$ | 10.1 | 0.237 | 0.0215 | 0.0181 | 0.0335 | 3.18 |
| | | | | | 19 | 0.332 | 0.0333 | 0.028 | 0.0518 | 3.15 |
| | | | | | 27.8 | 0.422 | 0.038 | 0.0323 | 0.0602 | 3.07 |
| | | | | | 35.4 | 0.467 | 0.0354 | 0.0304 | 0.0567 | 3.01 |
| 0.0627 | 0.036 | 0.0395 | 5.1 | $1.3 \times 10^5$ | 10.1 | 0.177 | 0.0154 | 0.0131 | 0.0243 | 3.63 |
| | | | | | 19 | 0.25 | 0.0229 | 0.0195 | 0.0362 | 3.63 |
| | | | | | 27.8 | 0.334 | 0.031 | 0.0262 | 0.0486 | 3.63 |
| | | | | | 35.4 | 0.394 | 0.0348 | 0.0297 | 0.0552 | 3.57 |

*Notes*: $Q$: flow rate; $h$: gate opening; $d_1$: water depth immediately upstream of the jump (measured at $x$ = 1.40 m); $Fr_1$: Froude number at $x$ = 1.40 m; $x$: longitudinal position; Re: Reynolds number; $\delta$: boundary layer thickness; $\delta_1$: displacement thickness; $\delta_2$: momentum thickness; $\delta_3$: energy thickness; $V_{max}$: free-stream velocity.

and above the flume centreline. The sensors included six Mic + 25/IU/TC with 0.18 mm accuracy and 50 ms response time, and one Mic + 35/IU/TC sensor with 0.18 mm accuracy and 70 ms response time. The locations of the sensors were fixed for all experiments: they are listed in Table 1 where $x$ is the longitudinal distance from the channel upstream end and $x_1$ is the hydraulic jump toe location. Each probe signal output was scanned at 50 Hz per sensor for 10 min. The sensors were calibrated on site before each day of experiments.

The displacement metre outputs included a few erroneous measurements when the angle between the free surface and horizontal was important and the reflected beam did not return to the acoustic displacement metre head. Another situation was when some air–water splashing was detected by the sensor instead of the free surface. This translated into spikes in the signals which were removed by a threshold technique.

#### 2.1.2. Two-phase flow measurements

The air–water flow properties were measured with a double-tip conductivity probe. The dual-tip probe was equipped with two identical sensors with an inner diameter of 0.25 mm. The distance between probe tips was $\Delta x_{tip}$ = 7.12 mm. The probe was manufactured at the University of Queensland. The dual-tip probe was excited by an electronic system (Ref. UQ82.518) designed with a response time of less than 10 μs. During the experiments, each probe sensor was sampled at 20 kHz for 45 s. The displacement and the position of the probe in the vertical direction were controlled by a fine adjustment system connected to a Mitutoyo™ digimatic scale unit with a vertical accuracy of less than 0.1 mm.

The analysis of the probe voltage output was based upon a single-threshold technique, with a threshold set at 50% of the air–water voltage range. The error on the void fraction was expected to be less than 1% using this technique. The single-threshold technique is a robust method that is well-suited to free-surface flows [8]. A number of air–water flow properties were derived from the probe signal analysis. These included the void fraction $C$ defined as the volume of air per unit volume of air and water, the bubble count rate or bubble frequency $F$ defined as the number of bubbles impacting the probe tip per second, and the air chord time distribution where the chord time is defined as the time spent by the bubble on the probe tip.

### 2.2. Inflow conditions

In the upstream supercritical flow, a turbulent boundary layer developed and its properties were investigated. For several discharges, the vertical distributions of velocity and pressure were measured with the Prandtl–Pitot tube for $0 < x < x_1$ = 1.50 m. All the experiments were carried out with the same upstream rounded gate opening $h$ = 0.036 m, for which the flow depth immediately upstream of the roller toe differed depending on the discharges, ranging from $d_1$ = 0.0395 m to 0.0440 m (Table 2, 3rd column).

The measurements showed that the pressure distributions were hydrostatic. The velocity profile measurements indicated that the supercritical flow was partially developed, consisting of a developing boundary layer and an ideal fluid flow region above (Fig. 3). For each flow condition, the boundary layer thickness, displacement, momentum and energy thicknesses were calculated (Table 2). The complete data set is reported in Table 2 (7–10th columns) together with the free-stream velocity $V_{max}$ (Table 2, 11th column). The boundary layer growth data were best correlated by:

$$\frac{\delta}{d_1} \propto \left(\frac{x - x_o}{d_1}\right)^{4/5} \quad (3)$$

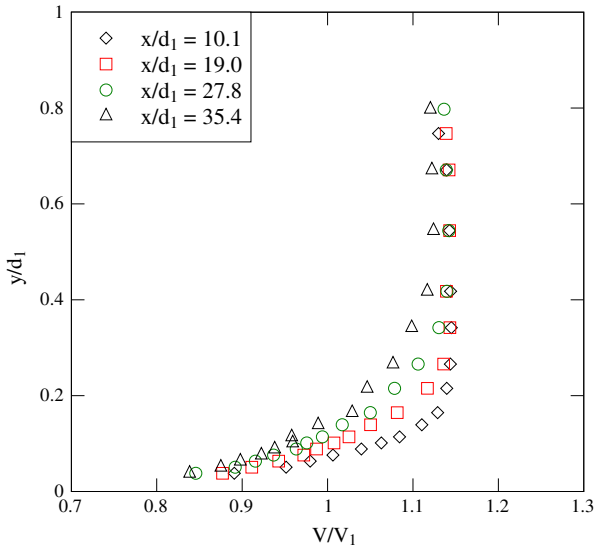


**Fig. 3.** Dimensionless velocity profiles in the developing flow upstream of the hydraulic jump for $Fr_1 = 5.1$, $d_1 = 0.0395$ m, $h = 0.036$ m, Re = $1.3 \times 10^5$.

where $\delta$ is the boundary layer thickness, $d_1$ is the water depth at the position $x = 1.40$ m, corresponding to a location immediately upstream of the jump toe for all the experiments conducted in this study, $x$ is the longitudinal distance from the upstream gate, and $x_o$ is the virtual origin of the boundary layer that was function of the flow conditions. For a wall jet configuration, the virtual origin $x_o$ of the boundary layer is usually not located at the opening but upstream of the gate (Schwarz and Cosart, 1964, [4]).

### 2.3. Experimental flow conditions

Two series of experiments were conducted. The first series focused on some basic observations of hydraulic jump properties and some detailed free-surface characteristics. The experiments were performed with Froude numbers between 2.4 and 5.1 corresponding to Reynolds numbers between $6.6 \times 10^4$ and $1.3 \times 10^5$. During the second series of experiments, the free-surface fluctuations and two-phase flow properties were recorded simultaneously. The upstream Froude numbers ranged between 3.8 and 5.1 and the Reynolds numbers between $9.8 \times 10^4$ and $1.1 \times 10^5$.

For both series of experiments, the upstream rounded gate opening was set at $h = 0.036$ m, and the jump toe was located at $x_1 = 1.50$ m. For these conditions, the inflow depth ranged from 0.042 down to 0.038 m depending upon the flow rate and the inflow conditions were partially-developed (Table 2).

## 3. Free-surface fluctuations

### 3.1. Free-surface profiles

For Froude numbers $Fr_1$ less than 2.4, the hydraulic jump was undular. That is, the front was followed by a train of secondary waves or undulations. For $Fr_1 > 2.4$, the jump had a marked breaking roller, with some increasing air entrainment and air–water projections with increasing Froude number (Fig. 2). For the remaining sections, the inflow Froude number $Fr_1$ was larger than or equal to 2.4, and thus corresponded to breaking jumps without undulations.

The longitudinal free-surface profiles were recorded for a series of Froude numbers ranging from 2.4 to 5.1 (Table 3). The instrumentation consisted in seven acoustic displacement metres located at different longitudinal positions (Table 1) and sampled simultaneously at 50 Hz for 10 min. Fig. 4A presents some typical mean free-surface profiles. In Fig. 4A, $\eta$ is the time-averaged free-surface elevation above the invert, $x$ is the longitudinal position of the sensor and $d_1$ is the inflow depth immediately upstream of the hydraulic jump toe. The data showed some longitudinal profiles that were very close to the photographic observations through the glass sidewalls. In a hydraulic jump, the flow properties immediately upstream and downstream of the jump roller must satisfy the continuity and momentum principles [9,12]. Eq. (1) shows the classical result in a rectangular, horizontal, smooth channel, and it is compared the present experimental data in Fig. 5 as well as with other data sets. The results showed a close agreement between the data and theory as expected.

The standard deviation of the water elevation $\eta'$ was recorded and Fig. 4B presents $\eta'/d_1$ as a function of the dimensionless distance from the jump toe $(x - x_1)/d_1$ for the same flow conditions as Fig. 4A. Basically, some small free-surface fluctuations were observed upstream of the jump toe ($x - x_1 < 0$). A significant increase in free-surface fluctuation was observed immediately downstream of the jump toe ($x - x_1 > 0$) for all Froude numbers, and the free-surface fluctuations reached a maximum value $\eta'_{max}$ within the roller. This maximum value $\eta'_{max}$ increased with increasing Froude numbers (Fig. 6). The large standard deviations in free-surface elevations were believed to be linked with a large number of air–water projections above the roller and jump toe. Further downstream, the free-surface fluctuations $\eta'$ decreased with increasing distance from the jump toe. The results were consistent with the earlier studies of Mouaze et al. [14], Kucukali and Chanson [11] and Murzyn and Chanson [15].

The peak of turbulent fluctuations was observed for $(x - x_1)/d_1 < 7$ (Fig. 4B). That is, the peak in turbulent free-surface fluctuations was located in the first half of the roller as previously observed by Mouaze et al. [14] and Murzyn and Chanson [15]. For example, the standard deviation of the free-surface elevation was nearly 0.6 times the inflow depth ($0.6d_1$) for $Fr_1 = 5.0$ (Fig. 4B).

**Table 3**
Experimental conditions of the free surface profile experiments (Present study).

| $Q$ (m$^3$/s) | $B$ (m) | $h$ (m) | $x_1$ (m) | $d_1$ (m) | $\delta$ (m) | $Fr_1$ | Re | $d_2$ (m) | $F_{fs}$ (Hz) |
|---|---|---|---|---|---|---|---|---|---|
| 0.033 | 0.50 | 0.036 | 1.50 | 0.0420 | – | 2.4 | $6.6 \times 10^4$ | 0.1247 | 2.1–5 |
| 0.0365 | 0.50 | 0.036 | 1.50 | 0.0425 | – | 2.7 | $7.3 \times 10^4$ | 0.1414 | 2.8–3.7 |
| 0.040 | 0.50 | 0.036 | 1.50 | 0.0438 | – | 2.8 | $8.0 \times 10^4$ | 0.1576 | 2.65–3 |
| 0.0446 | 0.50 | 0.036 | 1.50 | 0.0454 | 0.0051 | 2.9 | $8.9 \times 10^4$ | 0.1785 | 2.5–3 |
| 0.0468 | 0.50 | 0.036 | 1.50 | 0.0444 | – | 3.2 | $9.4 \times 10^4$ | 0.1870 | 1.6–3.8 |
| 0.049 | 0.50 | 0.036 | 1.50 | 0.0442 | 0.0055 | 3.4 | $9.8 \times 10^4$ | 0.1963 | 1.85–3.9 |
| 0.0515 | 0.50 | 0.036 | 1.50 | 0.0412 | – | 3.9 | $1.0 \times 10^5$ | 0.2068 | 1.7–2.9 |
| 0.0545 | 0.50 | 0.036 | 1.50 | 0.0430 | 0.0184 | 4.4 | $1.1 \times 10^5$ | 0.219 | 1.6–3.8 |
| 0.0573 | 0.50 | 0.036 | 1.50 | 0.0378 | – | 5.0 | $1.1 \times 10^5$ | 0.235 | 1.95–2.55 |
| 0.0627 | 0.50 | 0.036 | 1.50 | 0.0395 | 0.0156 | 5.1 | $1.3 \times 10^5$ | 0.257 | 1.8–2.4 |

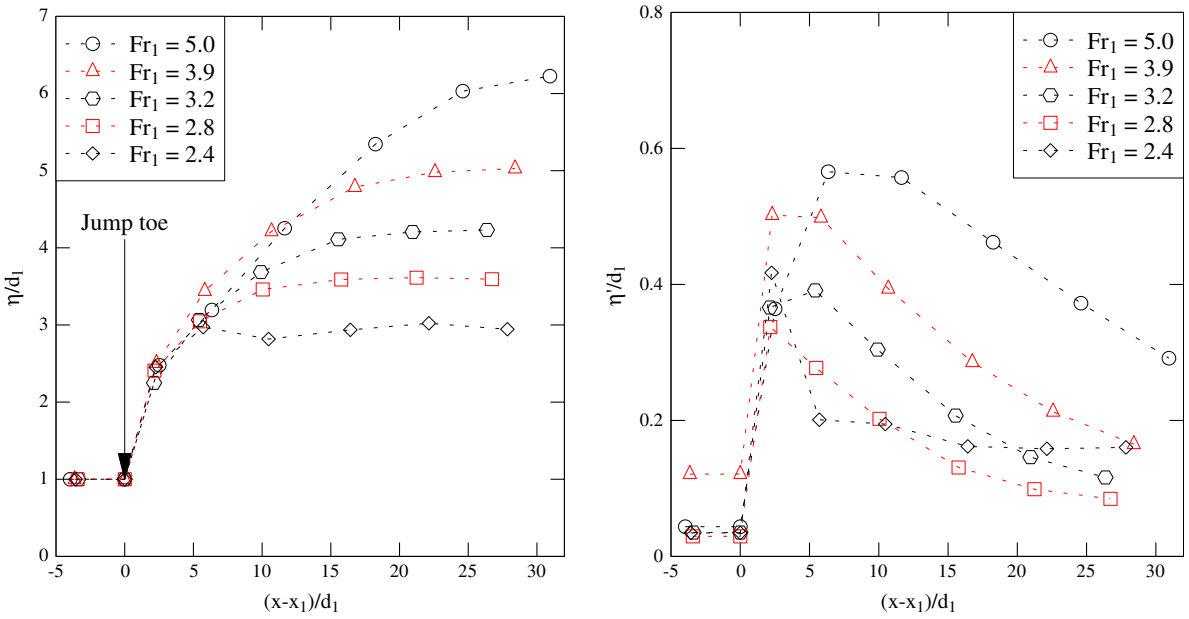


(A, Left) Dimensionless time-averaged free surface profile $\eta/d_1$

(B, Right) Dimensionless free surface fluctuations $\eta'/d_1$

**Fig. 4.** Free surface profile measurements in hydraulic jumps.

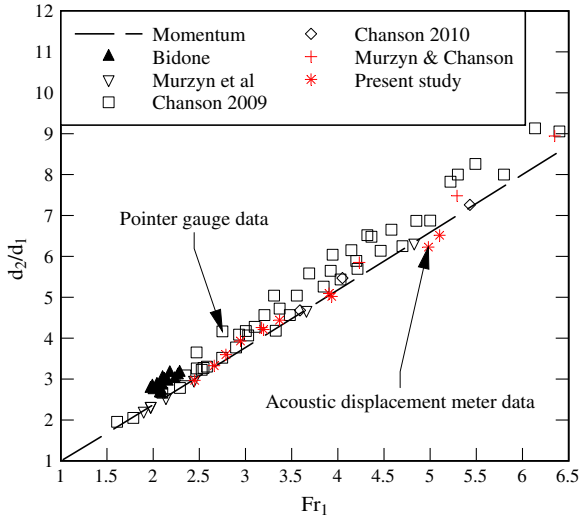


**Fig. 5.** Ratio of conjugate depths $d_2/d_1$ in hydraulic jumps – comparison between the momentum principle (Eq. (1)), experimental data obtained using acoustic displacement metres (Red symbols: [15], Present study) and data based upon pointer gauges (Black & white symbols: [2,16,6,7]).

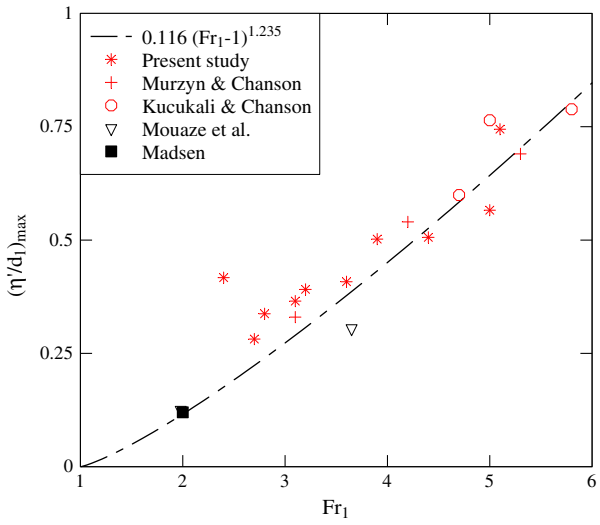


**Fig. 6.** Maximum of turbulent fluctuations $\eta'_{max}/d_1$ in hydraulic jumps as a function of Froude number $Fr_1$ – comparison between Eq. (4) and experimental data [11,13–15], Present study) – red symbols are acoustic displacement metre data. (For interpretation of the references to colour in this figure legend, the reader is referred to the web version of this article.)

The free surface profile became more turbulent with increasing Froude number. Fig. 6 summarises the dimensionless peak of turbulent fluctuations $\eta'_{max}/d_1$ as a function of the inflow Froude number. The present data are compared with the data fit proposed by Murzyn and Chanson [15]:

$$\left(\frac{\eta'}{d_1}\right)_{max} = 0.116\,(Fr_1 - 1)^{1.235} \quad (4)$$

Eq. (4) is shown in Fig. 6 together with the data. There is a good agreement, but for the lowest Froude number. The present data were further in close agreement with the data of Madsen [13], Mouaze et al. [14], Kucukali and Chanson [11] and Murzyn and Chanson [15] (Fig. 6).

### 3.2. Free-surface frequencies

A spectral analysis of the acoustic displacement metre signal outputs was performed. The results showed a dominant characteristic frequency between 1.6 and 4 Hz. Fig. 7A summarises the characteristic frequencies of the free-surface fluctuations in hydraulic jumps for Froude numbers, between 3.1 and 5.1, as a function of the dimensionless distance to the jump toe $(x - x_1)/d_1$. For some

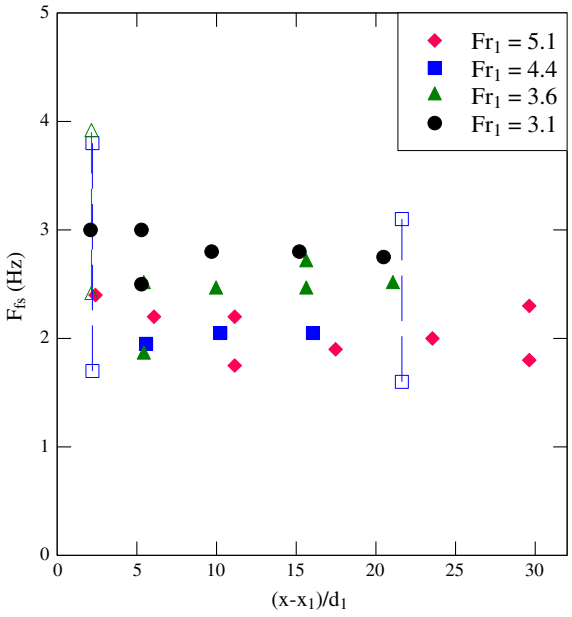


(A) Characteristic free-surface fluctuation frequency as a function of the longitudinal distance from the jump toe

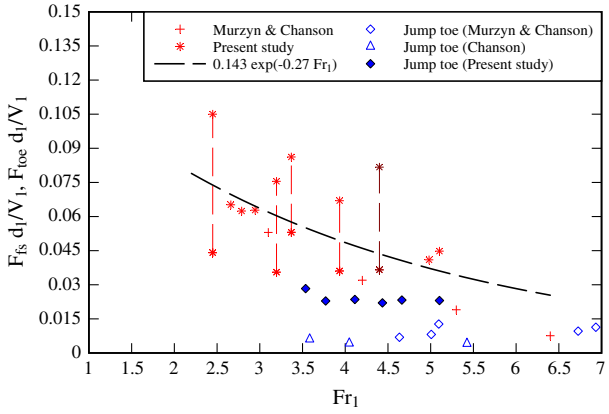


(B) Dimensionless free-surface fluctuation frequency $F_{fs}d_1/V_1$ as a function of the inflow Froude number - Comparison with the experimental data of MURZYN and CHANSON (2009) and Equation (5), and with jump toe fluctuations data (MURZYN and CHANSON 2009, CHANSON 2010, present study)

**Fig. 7.** Characteristic frequencies of the free-surface fluctuations of hydraulic jumps for Froude numbers between 2.4 and 5.1.

positions, the results indicated two characteristic frequencies. In these cases, both frequencies are shown on Fig. 7A. In other cases, the data presented a flat zone of maximum amplitude. For this situation, both ends of the range were recorded. These zones are represented on Fig. 7A in the form of two points linked with a dashed line. Overall the dominant frequencies showed relatively little effect of the longitudinal distance $(x - x_1)/d_1$ (Fig. 7A).

Fig. 7B shows the characteristic free-surface fluctuation frequency in the hydraulic jump roller as a function of the inflow Froude number. The data are shown with the range of data scatter and they are compared with the data of Murzyn and Chanson [15] obtained with the same instrumentation, sampling rate and sampling duration (50 Hz for 10 min). Despite some scatter, the data were close and showed a slight decrease in dimensionless free-surface frequency with increasing Froude number. Both data sets were best correlated by:

$$\frac{F_{fs}\, d_1}{V_1} = 0.143\ \exp(-0.27\, Fr_1) \quad 2.4 < Fr_1 < 6.5 \tag{5}$$

with a normalised correlation coefficient of 0.62. Eq. (5) is compared with the data in Fig. 7B.

The horizontal oscillations of the jump toe were recorded and the data are shown in Fig. 7B. The results are plotted in terms of a Strouhal number defined as $F_{toe}d_1/V_1$ where $F_{toe}$ is the jump toe oscillation frequency. They were compared with earlier jump toe oscillation data [15,7] and with the dimensionless free-surface fluctuation frequencies. Despite some scatter, the range of jump toe fluctuation frequency was lower than the free-surface fluctuation frequency observations particularly at small inflow Froude numbers (Fig. 7B). The finding differs from results in hydraulic jumps with large Froude numbers which showed similar jump toe fluctuation and free-surface fluctuation frequencies for $Fr_1 > 7$.

### 3.3. Longitudinal and transverse integral length and time scales

Some simultaneous free-surface measurements were performed to characterise the coherent turbulent structures located

next to the free surface. In the experimental setup, three acoustic displacement sensors were located above the free surface of the hydraulic jump (Fig. 2), and sampled simultaneously at 50 Hz for 60 s. For a given flow rate $Q$, the reference sensor was located at a longitudinal distance $(x - x_1)$ from the jump toe, and the experiment was repeated for a range of relative position of the two other sensors; these were separated from the reference sensor by the distance $\Delta x$ and $\Delta z$ respectively in the longitudinal and transverse directions (Fig. 2). The experiments were conducted for three different flow conditions (Table 4). The distances between the sensors, $\Delta x$ in the longitudinal direction and $\Delta z$ in the transverse direction, varied from 41 mm to 230 mm. Table 4 summarises the experimental conditions and Fig. 2 illustrates the experimental setup. The cross-correlation function between the signal outputs of the two sensors separated by $\Delta x$ in the longitudinal direction provided some information on the coherence of the free-surface fluctuations in the longitudinal flow direction. The correlation between the outputs of the two sensors separated transversely by $\Delta z$ yielded a similar information in the transverse direction. The level of correlations characterised the existence of coherent turbulent structures beneath and next to the free surface that could be described by some correlation length and time scales.

For each set of inflow conditions, and at every streamwise position $(x - x_1)$ of the reference sensor, the maximum values of the correlation functions $R_{xx',\max}$ and $R_{xz,\max}$ were recorded. The results showed that the relationships between the maximum cross-correlation coefficients $R_{xx',\max}$ and $R_{xz,\max}$ and the separation distances exhibited an exponential decay:

$$R_{xx',\max} = \exp\left(-1.204\frac{\Delta x/d_1}{(\Delta x/d_1)_{30}}\right) \quad (6)$$

$$R_{xz,\max} = \exp\left(-1.204\frac{\Delta z/d_1}{(\Delta z/d_1)_{30}}\right) \quad (7)$$

where $R_{xx',\max}$ is the maximum cross-correlation coefficient in the longitudinal direction, $R_{xz,\max}$ is the maximum cross-correlation coefficient in the transverse direction, and $(\Delta x/d_1)_{30}$ and $(\Delta z/d_1)_{30}$ are respectively the dimensionless separation distances for which $R_{xx',\max}$ and $R_{xz,\max}$ equal 30% of their maximum value. Note that for $\Delta x = \Delta z = 0$, $R_{xx',\max} = R_{xz,\max} = 1$. Fig. 8 presents a comparison between Eq. (6) and the experimental results. The normalised correlation coefficient between the data and Eqs. (6) and (7) were 0.953 and 0.959 respectively.

The characteristic parameters $(\Delta x/d_1)_{30}$ and $(\Delta z/d_1)_{30}$ were functions of the Froude number $Fr_1$ and of the longitudinal distance from the jump toe $(x - x_1)/d_1$. The experimental results are presented in Fig. 9. Basically, $(\Delta x/d_1)_{30}$ and $(\Delta z/d_1)_{30}$ increased both with an increasing distance from the jump toe $(x - x_1)/d_1$. The results suggested that the flow region with a cross-correlation coefficient of the free-surface fluctuations greater than 0.3 enlarged

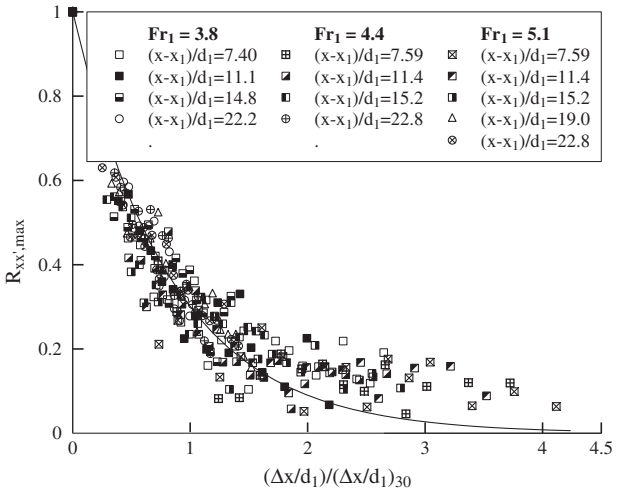


**Fig. 8.** Maximum cross-correlation coefficient $R_{xx',\max}$ as a function of the longitudinal separation distance $\Delta x$ – comparison with Eq. (6).

with increasing distance from the jump toe. Further, $(\Delta x/d_1)_{30}$ yielded higher values than $(\Delta z/d_1)_{30}$. That is, the fluctuations of the free surface were better correlated in the longitudinal direction than in the transverse direction.

The correlation functions of the free-surface fluctuations were linked with some coherence of the large vortical structures interacting with the free surface. Based upon the correlation analyses, some quantitative turbulent properties were derived including integral length and time scales. The maximum cross-correlation coefficient $R_{xx',\max}$ and $R_{xz,\max}$ results were used to calculate the free surface integral length scales $L_{xx'}$ and $L_{xz}$, defined as:

$$L_{xx'} = \int_0^{\Delta x_{\max}} R_{xx',\max}(X)\, dX \quad (8)$$

$$L_{xz} = \int_0^{\Delta z_{\max}} R_{xz,\max}(Z)\, dZ \quad (9)$$

where $X$ and $Z$ are respectively the longitudinal and transverse separation distances, and $\Delta x_{\max}$ and $\Delta z_{\max}$ represent the upper limit of the sensor separation ($\Delta x_{\max} = \Delta z_{\max} = 230$ mm herein, Table 4). Fig. 10 presents the integral length scales $L_{xx'}$ and $L_{xz}$ as functions of the distances from the jump toe. The experimental results showed that the free-surface length scales increased with increasing distance from the jump toe. For a streamwise position $(x - x_1)/d_1$ from 7 to 23, the longitudinal length scale $L_{xx'}$ ranged from $1.2d_1$ to $3.5d_1$. The transverse length scale $L_{xz}$ ranged from $1.2d_1$ to $2.6d_1$ for streamwise positions $(x - x_1)/d_1$ between 2 and

**Table 4**
Experimental conditions of the length and time scale experiments and simultaneous measurements of free-surface fluctuations and air–water flow properties (Present study).

| $Q$ (m$^3$/s) | $B$ (m) | $h$ (m) | $x_1$ (m) | $d_1$ (m) | $\delta$ (m) | $x - x_1$ (m) | $\Delta x$ (mm) | $\Delta z$ (mm) | $Fr_1$ | Re |
|---|---|---|---|---|---|---|---|---|---|---|
| 0.049 | 0.50 | 0.036 | 1.50 | 0.0405 | 0.0055 | 0.150<br>0.300<br>0.450 | 41–30 | 41–30 | 3.8 | $9.8 \times 10^4$ |
| 0.0545 | 0.50 | 0.036 | 1.50 | 0.0395 | 0.0184 | 0.150<br>0.300<br>0.450 | 41–30 | 41–30 | 4.4 | $1.1 \times 10^5$ |
| 0.0627 | 0.50 | 0.036 | 1.50 | 0.0395 | 0.0156 | 0.150<br>0.300<br>0.450 | 41–30 | 41–30 | 5.1 | $1.3 \times 10^5$ |

*Note*: $Q$: flow rate; $B$: channel width; $h$: gate elevation; $x_1$: longitudinal position of the jump toe; $d_1$: water depth immediately upstream of the jump toe; $\delta$: inflow boundary layer thickness (at $x = 1.4$ m); $\Delta x$: longitudinal separation distance between the sensors; $\Delta z$: transverse separation distance; $Fr_1$: upstream Froude number; Re: Reynolds number; $x$: longitudinal position of the investigated cross-sections (streamwise position).

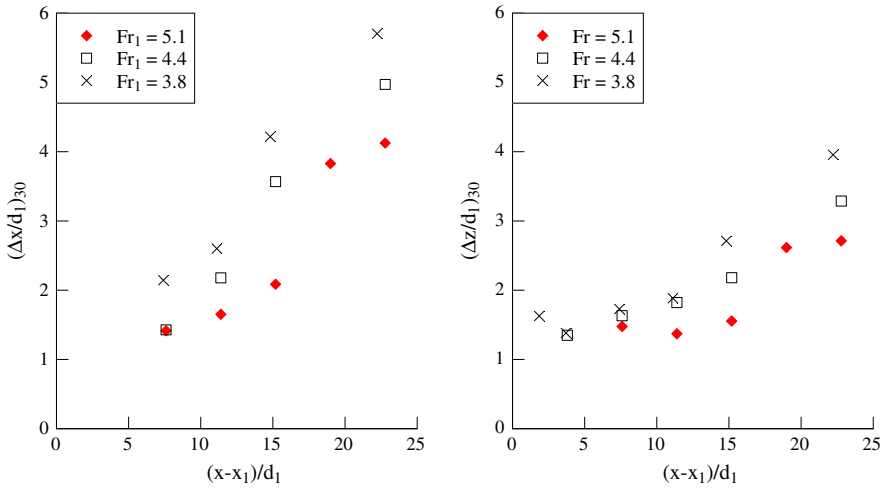


**Fig. 9.** Characteristic parameters $(\Delta x/d_1)_{30}$ (Left side) and $(\Delta z/d_1)_{30}$ (Right side) as functions of the dimensionless distance $(x - x_1)/d_1$ from the jump toe.

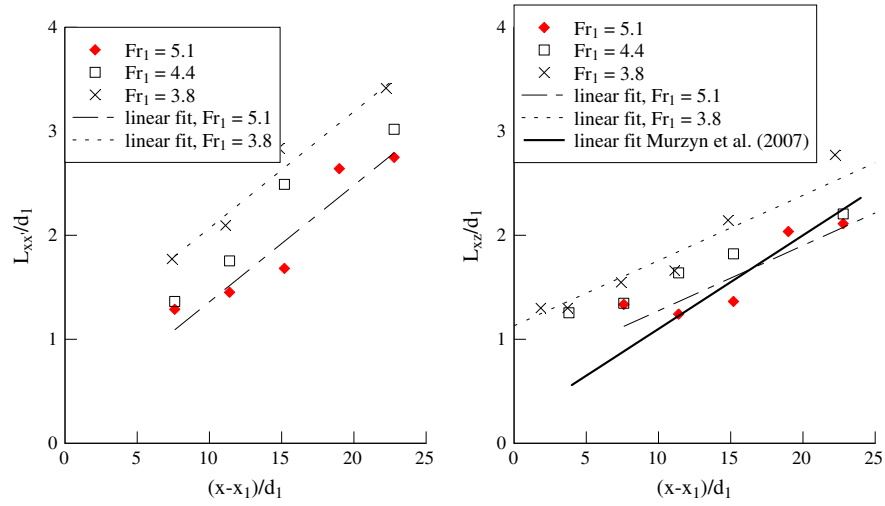


(A, Left) Longitudinal free surface integral length scales

(B, Right) Transverse free surface integral length scales

**Fig. 10.** Longitudinal and transverse free surface integral length scales – comparison between experimental data and Eqs. (8) and (9).

23. The results were linked with the inflow Froude number $Fr_1$ and the present data were best fitted by:

$$\frac{L_{xx'}}{d_1} = 0.112\frac{x - x_1}{d_1} + (3.02 - 0.545\,Fr_1) \quad 3.8 < Fr_1 < 5.1 \tag{10}$$

$$\frac{L_{xz}}{d_1} = 0.0627\frac{x - x_1}{d_1} + (2.54 - 0.371\,Fr_1) \quad 3.8 < Fr_1 < 5.1 \tag{11}$$

At a given longitudinal location, the longitudinal integral length scale $L_{xx'}$ was slightly larger than the transverse length scale $L_{xz}$. The result implied that the turbulence was not homogeneous at the free surface of the hydraulic jump. The transverse length scale data were compared to the linear fit of Murzyn et al. [16] who performed similar free-surface measurements with resistive probes (Fig. 10B). Fig. 10B, indicates some agreement between the present data and their data, but close to the jump toe: i.e., for $(x - x_1)/d_1 > 10$. In the present study, some larger transverse length scales $L_{xz}$ were observed close to the jump toe ($(x - x_1)/d_1 < 10$).

The variations of the integral length scales $L_{xx'}$ and $L_{xz}$ were linked to those of $(\Delta x/d_1)_{30}$ and $(\Delta z/d_1)_{30}$ (Eqs. (6) and (7)). This is indeed a consequence of the self-similarity of maximum cross-correlation coefficient distributions. Combining Eqs. (6) and (7) with Eqs. (8) and (9), the following theoretical relationships may be derived:

$$\frac{L_{xx',theory}}{d_1} = \frac{(\Delta x/d_1)_{30}}{1.204}\left(1 - \exp\left(-1.204\frac{\Delta x_{max}/d_1}{(\Delta x_{max}/d_1)_{30}}\right)\right) \tag{12}$$

$$\frac{L_{xz,theory}}{d_1} = \frac{(\Delta z/d_1)_{30}}{1.204}\left(1 - \exp\left(-1.204\frac{\Delta z_{max}/d_1}{(\Delta z_{max}/d_1)_{30}}\right)\right) \tag{13}$$

The integral length scales $L_{xx'}$ and $L_{xz}$ are proportional to $(\Delta x/d_1)_{30}$ and $(\Delta z/d_1)_{30}$ respectively, notwithstanding for some correction to account for $\Delta x_{max}$ and $\Delta z_{max}$ not being infinity. When $\Delta x_{max}$ and $\Delta z_{max}$ tend to infinity, Eqs. (12) and (13) become respectively:

$$\frac{L_{xx',theory}}{d_1} = \frac{1}{1.204}(\Delta x/d_1)_{30} \quad \Delta x_{max} \to +\infty \tag{14}$$

$$\frac{L_{xz,theory}}{d_1} = (\Delta z/d_1)_{30} \quad \Delta z_{max} \to +\infty \tag{15}$$

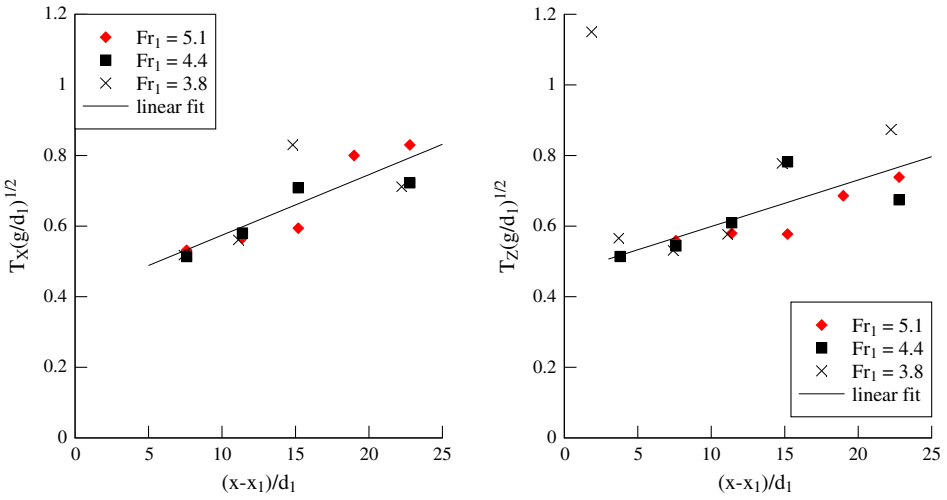


(A) Evolution of $T_X$ along the jump (B) Evolution of $T_Z$ along the jump

**Fig. 11.** Longitudinal and transverse integral time scales as functions of the longitudinal distances from the jump toe – comparison with Eqs. (20) and (21).

The evolution of $L_{xx'}$ and $L_{xz}$ would then be proportional to $(\Delta x/d_1)_{30}$ and $(\Delta z/d_1)_{30}$, whose evolutions are presented in Fig. 9. A comparison between Figs. 9 and 10 shows the close agreement in trends.

*3.3.1. Integral time scales*

The analysis of the longitudinal and transverse cross-correlation functions provided some information on the free surface turbulence time scales. For each separation distance, $\Delta x$ or $\Delta z$, between the sensors, the correlation time scales $T_{xx'}$ and $T_{xz}$ were calculated as:

$$T_{xx'} = \int_{\tau=\tau(R_{xx'}=R_{xx',max})}^{\tau=\tau(R_{xx'}=0)} R_{xx'}(\tau)\, d\tau \quad (16)$$

$$T_{xz} = \int_{\tau=\tau(R_{xz}=R_{xz,max})}^{\tau=\tau(R_{xz}=0)} R_{xz}(\tau)\, d\tau \quad (17)$$

where $\tau$ is a time lag. $T_{xx'}$ represents a time scale characteristic of the free surface coherent structures on a length span $\Delta x$ in the longitudinal direction. $T_{xz}$ is a characteristic time of the free surface coherent structures in the transverse direction on a length span $\Delta z$.

The correlation time scales were used to estimate the turbulent integral time scales $T_X$ and $T_Z$:

$$T_X = \frac{1}{L_{xx'}} \int_{X=0}^{X=\Delta x_{max}} R_{xx',max} T_{xx'}\, dX \quad (18)$$

$$T_Z = \frac{1}{L_{xz}} \int_{Z=0}^{Z=\Delta z_{max}} R_{xz,max} T_{xz}\, dZ \quad (19)$$

where $X$ and $Z$ are the separation distances respectively in the longitudinal and transverse directions. The turbulent integral time scale $T_X$ represents the time scale of large free surface structures in the longitudinal direction. It integrates in space the correlation time scales at each position $\Delta x$, weighted by the maximum cross-correlation coefficient $R_{xx',max}$. $T_Z$ represents the time scale of large free surface structures in the transverse direction.

The experimental data in terms of the integral time scales $T_X$ and $T_Z$ are presented in Fig. 11. In Fig. 11 the term $(d_1/g)^{1/2}$ represents a characteristic time of the free surface flow. Despite some scatter, the data exhibited a linear increase in integral turbulent time scales with increasing distance from the jump toe. The trend was possibly linked with an increase in large coherent structure sizes and slower convection velocities with increasing distance from the jump toe. The data were further independent of the Froude and Reynolds numbers within the range of the experimental conditions (Table 4). Overall the integral turbulent time scales were best correlated by:

$$T_X\sqrt{\frac{g}{d_1}} = 0.4026 + 0.0172\frac{x - x_1}{d_1} \quad (20)$$

$$T_Z\sqrt{\frac{g}{d_1}} = 0.4670 + 0.0132\frac{x - x_1}{d_1} \quad (21)$$

with a normalised correlation coefficient of 0.82 and 0.78 respectively. The integral time scales were observed to be very similar in the longitudinal and transverse directions, although the integral length scale data showed differences between transverse and longitudinal results (Fig. 10). Eqs. (20) and (21) are compared with the experimental data in Fig. 11A and 11B respectively.

## 4. Simultaneous free surface and void fraction measurements

### 4.1. Presentation

In open channel flows with large free-surface fluctuations, the free surface deformations and discontinuity cause some air entrapment. Hornung et al. [10] detailed how this phenomenon generates vorticity. Murzyn and Chanson [15] conducted the first simultaneous measurements of free surface and void fraction fluctuations.

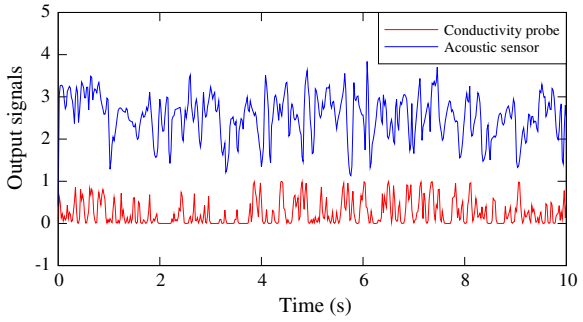


**Fig. 12.** Output signals of the conductivity probe (lower) and acoustic displacement metre (upper) after filtering and processing – flow conditions: $d_1 = 0.0405$ m, $x_1 = 1.50$ m, $Fr_1 = 3.8$, $Re = 8.9 \times 10^4$.

In the present study, new experiments are presented using the experimental technique of Murzyn and Chanson [15], but for different flow conditions (Table 4).

The air–water flow properties and free-surface fluctuations were measured simultaneously using an acoustic displacement metre Mic + 25/IU/TC and the double-tip conductivity probe. The two instruments were located on the centreline of the channel and vertically aligned: that is, the centre of the acoustic displacement metre sampling surface was aligned vertically with the conductivity probe leading tip. For each longitudinal position ($x - x_1$), several records were performed for different vertical elevations of the conductivity probe sensor. The acoustic sensor and the conductivity probe were sampled simultaneously at 5 kHz for 45 s. The same signal processing method was applied to the output signals of the sensors. The raw output signal of the conductivity probe was converted into a binary file of instantaneous void fraction being 0 for water and 1 for air. The signal was then filtered using a band pass 0–25 Hz. The filtering aimed to remove any electrical noise and high-frequency signal component with a frequency greater than the dynamic response of the sensor. The low-pass filtered signal was averaged over 100 points. The output was then linearly interpolated using a constant interval time 0.02 s to facilitate the correlation analysis. (The technique was identical to that developed by Murzyn and Chanson [15], but it was applied herein to the 45 s long signals, instead of 12 s long signals.). Fig. 12 shows an example of filtered output signals of the conductivity probe and the acoustic sensor.

### 4.2. Results

The analysis of the cross-correlation functions between the instantaneous void fraction $C_{inst}$ and instantaneous vertical elevation $\eta_{inst}$ exhibited two different trends depending upon the vertical elevation $y$ of the conductivity probe sensor. When the conductivity probe sensor was located in the upper part of the flow ($y/d_1 > 2$), the peak in cross-correlation for zero time lag was negative (Fig. 13A), while this peak was positive for $y/d_1 < 2$ (Fig. 13B). Fig. 13A presents a typical cross-correlation function between the probe output (leading tip) and the displacement sensor output, when the conductivity probe sensor was located in the upper part of the flow: i.e., the peak for zero time lag was negative. At a vertical location above the "mean" free-surface elevation measured by the acoustic sensor, an increase in instantaneous void fraction $C_{inst}$ characterised a void and was associated with a decrease in instantaneous free-surface elevation $\eta_{inst}$, hence the negative correlation. The result was observed systematically for $3.8 < Fr_1 < 5.1$.

Fig. 13B presents a typical cross-correlation function when the conductivity probe sensor was located in the lower flow region ($y/d_1 < 2$). Note the positive peak in the correlation function for zero time lag. An increase in instantaneous void fraction was linked with an increase in free-surface elevation. The cross-correlation function between free-surface elevation and instantaneous void fraction thus exhibited a positive peak. Note that the results exhibited significant cross-correlation functions at low elevations, only at the closest locations to the jump toe. These locations were: $(x - x_1)/d_1 = 3.70$ for $Fr_1 = 3.8$, $(x - x_1)/d_1 = 3.80$ for $Fr_1 = 4.4$ and $(x - x_1)/d_1 = 3.80$ for $Fr_1 = 5.1$. These regions of positive correlations corresponded to the developing shear layer in the breaking jump. Note further that the cross-correlation functions exhibited some quasi-periodic patterns with increasing time lag as observed by Murzyn and Chanson [15].

Overall, the cross-correlation function exhibited a tendency to be negative. It was assumed to be caused by the slow longitudinal fluctuations of the position of the jump toe. If the toe moved forward, the free-surface elevation at a position downstream of the toe increased, and the void fraction at a given vertical elevation decreased, hence a negative correlation. This phenomenon happened at a low frequency: it did not affect the instantaneous fluctuations of the cross-correlation function but added a negative constant to it.

The maximum values $R_{\eta C,max}$ of the cross-correlation functions between the instantaneous void fraction $C_{inst}$ and free-surface elevations $\eta_{inst}$ were recorded. These gave some measure of the peak amplitude. For example, $R_{\eta C,max} = -0.42$ in Fig. 13A and $R_{\eta C,max} = +0.15$ in Fig. 13B. Fig. 14 presents the vertical distribution of the

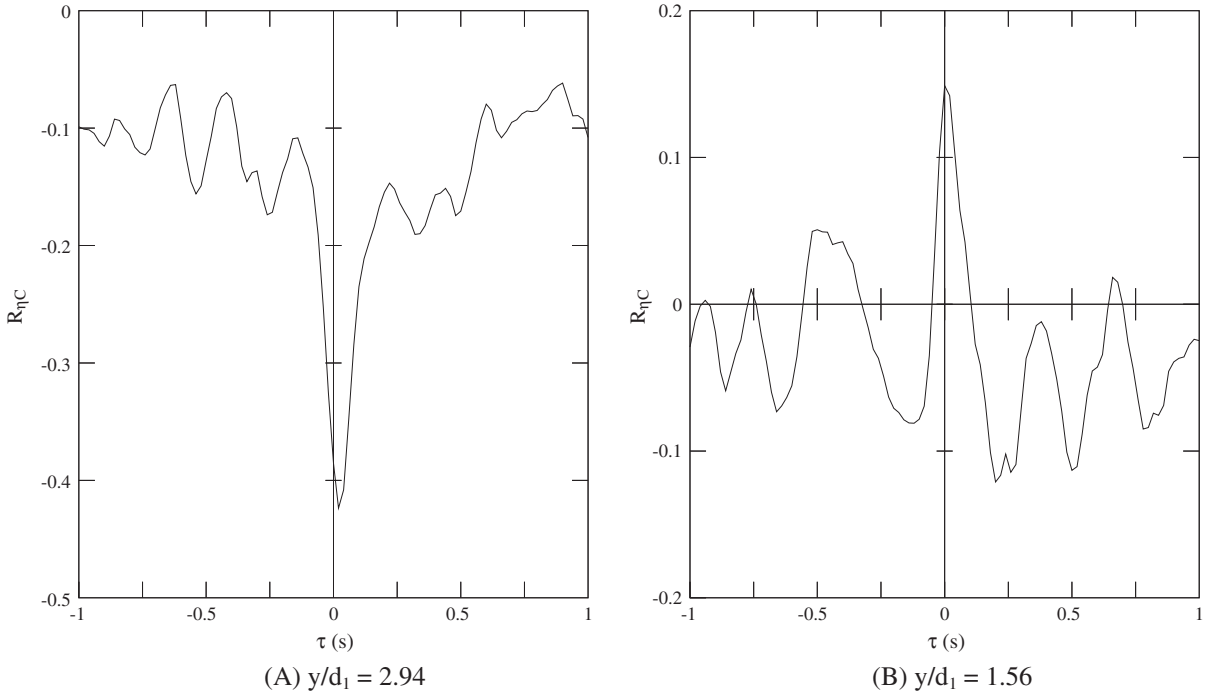


**Fig. 13.** Cross-correlation functions $R_{\eta C}$.: (A) in upper part of the flow (foam and splashing region) and (*B*) in the lower part of the flow (i.e. developing shear layer) – flow conditions: $d_1 = 0.0405$ m, $x_1 = 1.50$ m, $(x - x_1)/d_1 = 3.70$, $Fr_1 = 3.8$, Re = $8.9 \times 10^4$.

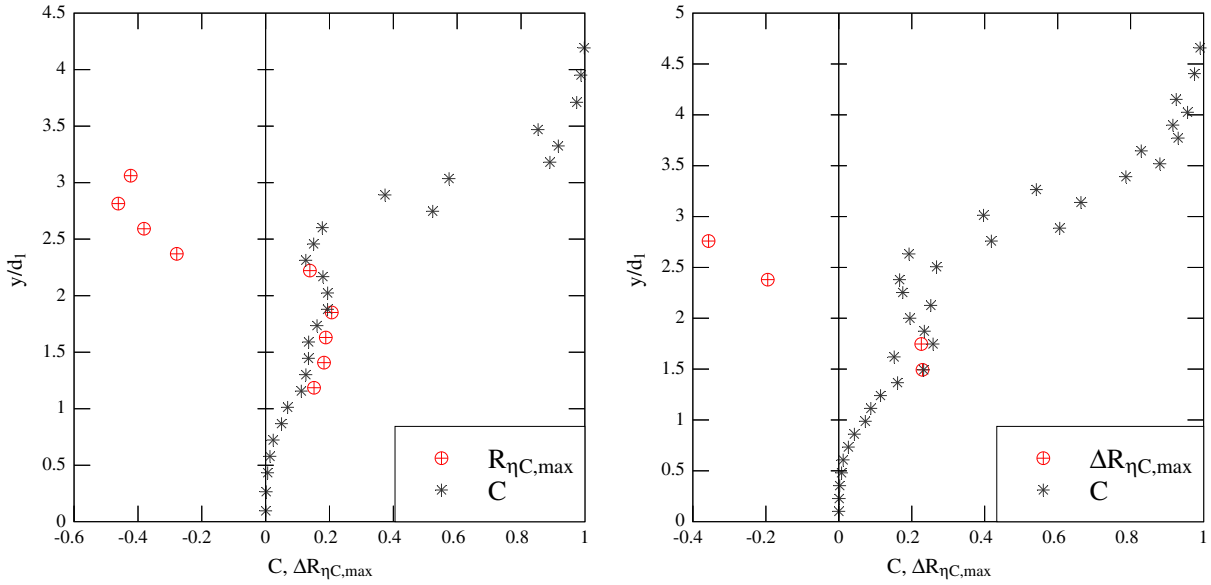


(A, Left) $d_1 = 0.0405$ m, $x_1 = 1.50$ m, $(x-x_1)/d_1 = 3.70$, $Fr_1 = 3.8$, $Re = 9.8\times10^4$

(B, Right) $d_1 = 0.0395$ m, $x_1 = 1.50$ m, $(x-x_1)/d_1 = 3.80$, $Fr_1 = 4.4$, $Re = 1.1\times10^5$

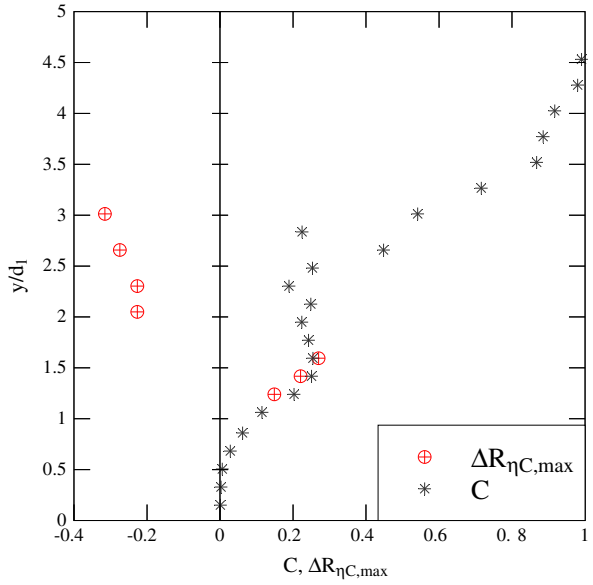


(C) $d_1 = 0.0395$ m, $x_1 = 1.50$ m, $(x-x_1)/d_1 = 3.80$, $Fr_1 = 5.1$, $Re = 1.3\times10^5$

**Fig. 14.** Vertical distributions of $\Delta R_{\eta C,max}$ and void fraction in hydraulic jump rollers.

maximum cross-correlation difference $\Delta R_{\eta C,max}$ at a longitudinal position close to the jump toe for different Froude numbers. $\Delta R_{\eta C,max}$ represents the jump in maximum cross-correlation function from its otherwise average value: for example, $\Delta R_{\eta C,max} = -0.32$ in Fig. 13A and $\Delta R_{\eta C,max} = +0.25$ in Fig. 13B. In Fig. 14, the time-averaged void fraction data are plotted also on each graph. Fig. 14 shows clearly the positive values of $\Delta R_{\eta C,max}$, in the lower elevations (i.e. air–water shear layer) and the negative values in the upper flow region (upper free-surface region).

### 4.3. Discussion

A key query is the physical significance of the time-averaged free-surface elevation $\eta$ measured by the acoustic displacement metres. While the acoustic displacement metre technique was robust, simple and non-intrusive, the sensors were not designed to detect a highly aerated, dynamic free-surface. Murzyn and Chanson [15] argued that the time-averaged free-surface elevation $\eta$ characterised the upper free-surface region ($\eta > y^*$, Fig. 15) that was typically a thin layer where the void fraction was basically larger than 20%, increasing monotonically towards unity.

A comparative analysis was conducted between the acoustic displacement metre and void fraction data. The time-averaged free-surface elevation recorded with the acoustic displacement metre was compared with the void fraction profile measured with the leading tip of the dual-tip conductivity probe. Some results are presented on Fig. 16A where $y_{Cmax}$ is the vertical elevation where $C = C_{max}$, $y^*$ is defined as the boundary between the turbulent shear

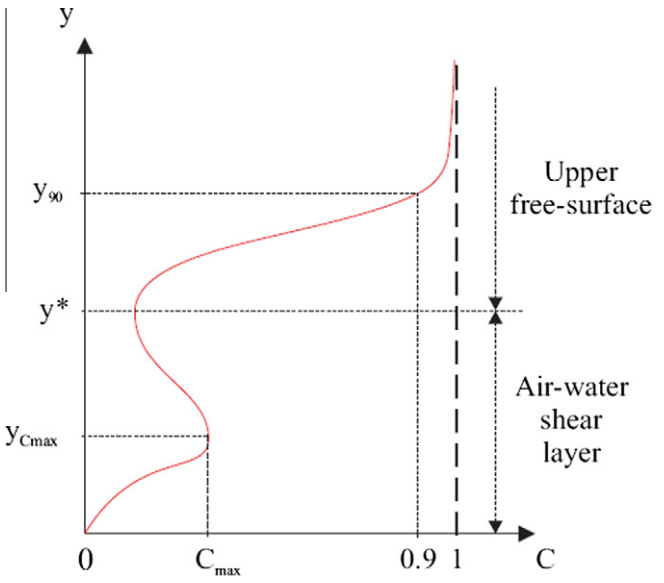


**Fig. 15.** Sketch of the vertical distribution of void fraction in the hydraulic jump roller.

layer and the upper part of the flow dominated by free surface strong fluctuations, and $y_{90}$ is the characteristic elevation where $C = 90\%$ (see definition in Fig. 15). The data (Fig. 16A) showed that the free-surface measurement $\eta$ of the acoustic displacement sensor was slightly above the characteristic location $y^*$ for all investigated Froude numbers and that:

$$1 < \frac{y_{C\max}}{d_1} < \frac{y^*}{d_1} < \frac{\eta}{d_1} < \frac{y_{90}}{d_1} \quad (22)$$

where $d_1$ is the upstream flow depth. The results showed that the free-surface elevation measured by the acoustic displacement sensor was within the upper free-surface region. This region was typically a thin air–water layer in which the void fraction increased rapidly from 20% to 90%. The present findings complemented the results of Murzyn and Chanson [15], and Eq. (22) narrowed the physical measure of the free-surface location in hydraulic jump ($y^* < \eta < y_{90}$) (Fig. 16A). Importantly the findings were found to be valid over a wide range of turbulent hydraulic jumps with Froude numbers between 3.1 and 8.5. The time-averaged free-surface elevation data $\eta$ was further compared with the equivalent clear-water depth $d$ deduced from the void fraction distribution:

$$d = \int_0^{y_{90}} (1 - C)\, dy \quad (23)$$

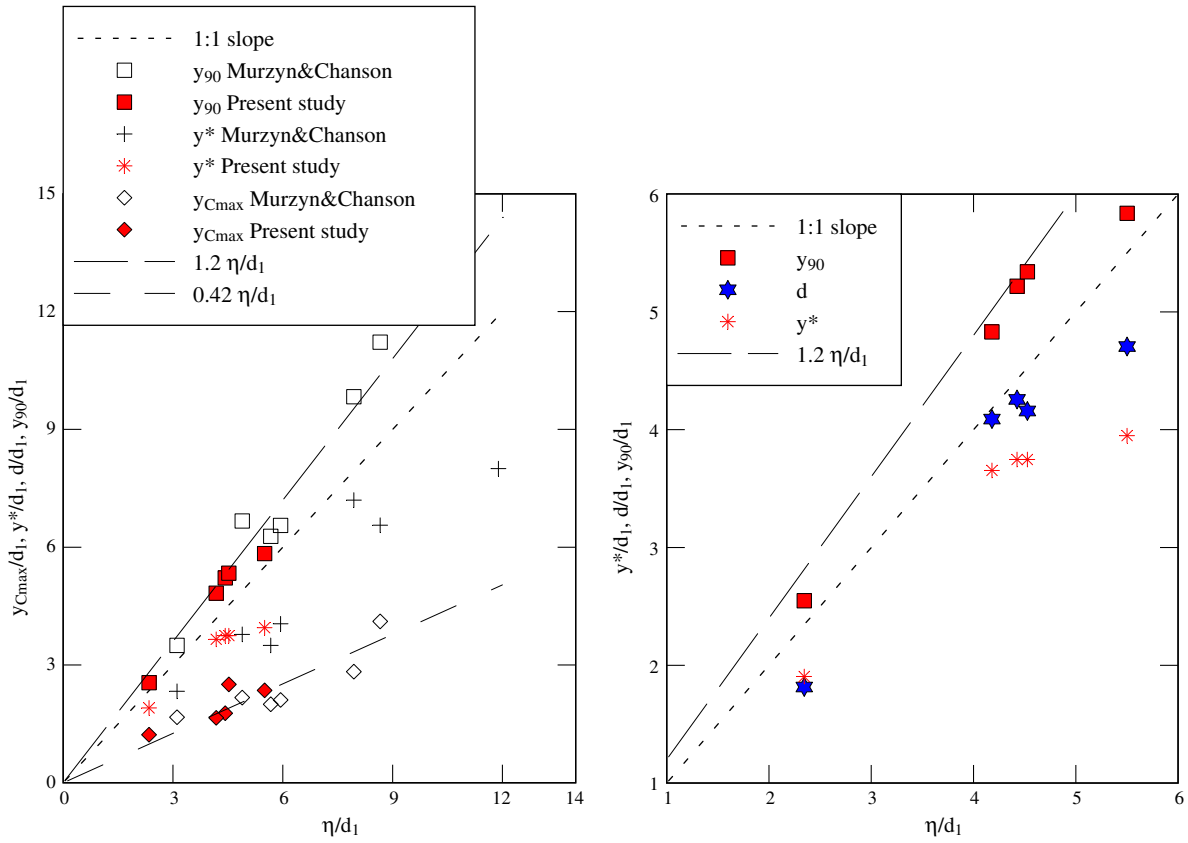


(A, Left) Comparison of acoustic displacement sensor and phase-detection conductivity probe data - Data: Present study (Red symbols, $3.1 < Fr_1 < 5.1$), MURZYN and CHANSON (2009) (Black symbols, $5.1 < Fr_1 < 8.5$)

(B, Right) Comparison of free surface elevation η and equivalent clear water depth d (Present study, $3.1 < Fr_1 < 5.1$)

**Fig. 16.** Comparison of free surface and void fraction measurements using acoustic displacement sensor and phase-detection conductivity probe respectively.

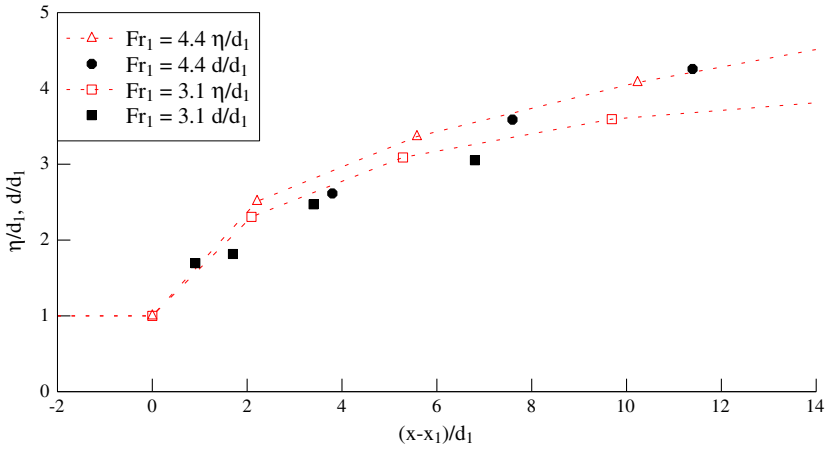


**Fig. 17.** Dimensionless longitudinal free-surface profiles of hydraulic jumps: comparison between the time-averaged free-surface elevation $\eta/d_1$ and equivalent clear-water depth $d/d_1$ for $Fr_1$ = 3.1 and 4.4.

The results are presented in Fig. 16B for the present data set. Note that the characteristic elevation $y^*$ and $y_{90}$ are also reported in Fig. 16B for completeness. The results showed a close agreement between the equivalent clear-water depth deduced from the void fraction distribution (Eq. (23)) and the time-averaged free-surface elevation $\eta$ measured with the acoustic displacement metre. This is illustrated in Fig. 17 for two upstream Froude numbers. Overall the approximation $\eta \approx d$ was correlated with a normalised coefficient of 0.97 for the entire data set ($3.1 < Fr_1 < 5.1$, Table 4).

## 5. Conclusion

The present study focused on the free-surface fluctuations and air–water properties in hydraulic jumps with relatively small Froude numbers ($2.4 < Fr_1 < 5.1$) and relatively large Reynolds numbers ($6.6 \times 10^4 < Re < 1.3 \times 10^5$). The experimental work complemented the earlier physical studies of Murzyn et al. [16] performed with similar Froude numbers and comparatively lower Reynolds numbers, and of Murzyn and Chanson [15] with larger Froude numbers and smaller Reynolds numbers. The dynamic free-surface measurements were performed with several non-intrusive sensors, namely acoustic displacement metres, to record the mean and turbulent surface profiles, characteristic frequencies, and integral length and time scales. The air–water flow measurements were conducted with a dual-tip conductivity probe. Some measurements of free-surface fluctuations and two-phase properties were conducted simultaneously, and a correlation analysis was conducted.

The free surface data indicated that the shape of the mean free surface profile was well defined and in agreement with visual and photographic observations. The turbulent fluctuation profiles exhibited a maximum in standard deviations in the first part of the hydraulic jump roller. Its amplitude increased monotically with increasing Froude number. The free-surface fluctuations exhibited some characteristic frequencies between 1.4 and 4 Hz, with the majority below 3 Hz. Some simultaneous free-surface measurements at a series of two closely located points yielded the free-surface length and time scales of free-surface fluctuations in terms of both longitudinal and transverse directions. The maximum cross-correlation coefficient between the free-surface fluctuations at two different locations decreased exponentially with increasing distance between the sensors. The integral length and time scales increased with increasing longitudinal distances from the jump toe, and the longitudinal length scales were greater than the transverse length scales. The length scale data seemed to depend upon the inflow Froude number, while the time scale data showed no definite trend.

The simultaneous measurements of instantaneous void fraction and free-surface fluctuations exhibited different features depending upon the phase-detection probe sensor location in the different regions of the roller: a positive correlation in the shear layer region, and a negative correlation in the free-surface region. The acoustic displacement metres yielded a time-averaged free-surface elevation that corresponded to the upper free-surface region where the void fraction increased rapidly from 0.20 to 0.90, and the quantitative values were very close to the equivalent clear-water depth.

## Acknowledgments

The authors thank Dr. Frédéric Murzyn (ESTACA Laval) for his valuable inputs. They thank Graham Illidge, Clive Booth, and Ahmed Ibrahim (The University of Queensland) for the technical assistance. The financial support of the Australian Research Council (Grant DP0878922) is acknowledged.

## References

[1] J.B. Bélanger, «Notes sur l'Hydraulique.» ('Notes on Hydraulic Engineering.') Ecole Royale des Ponts et Chaussées, Paris, France, session 1841–1842, 1841, 223 p (in French).
[2] G. Bidone, «Le Remou et sur la Propagation des Ondes.» ('The Jump and on the Wave Propagation.') Report to Académie Royale des Sciences de Turin, Séance 12 December, vol. XXV, 1819, pp. 21–112 and 4 plates (in French).
[3] Y. Chachereau, H. Chanson, Free-Surface Turbulent Fluctuations and Air–Water Flow Measurements in Hydraulics Jumps with Small Inflow Froude Numbers, Hydraulic Model Report No. CH78/10, School of Civil Engineering, The University of Queensland, Brisbane, Australia, 2010, 133 p.
[4] H. Chanson, Air bubble entrainment in open channels. Flow structure and bubble size distributions, International Journal of Multiphase Flow 23 (1) (1997) 193–203.
[5] H. Chanson, Bubbly flow structure in hydraulic jump, European Journal of Mechanics B/Fluids 26 (3) (2007) 367–384, doi:10.1016/j.euromechflu.2006.08.001.
[6] H. Chanson, Development of the Bélanger Equation and Backwater Equation by Jean-Baptiste Bélanger (1828), Journal of Hydraulic Engineering ASCE 135 (3) (2009) 159–163, doi:10.1061/(ASCE)0733-9429(2009)135:3(159).
[7] H. Chanson, Convective transport of air bubbles in strong hydraulic jumps, International Journal of Multiphase Flow 36 (10) (2010) 798–814, doi:10.1016/j.ijmultiphaseflow.2010.05.006.
[8] H. Chanson, G. Carosi, Advanced post-processing and correlation analyses in high-velocity air–water flows, Environmental Fluid Mechanics 7 (6) (2007) 495–508, doi:10.1007/s10652-007-9038-3.
[9] F.M. Henderson, Open Channel Flow, MacMillan Company, New York, USA, 1966.

[10] H.G. Hornung, C. Willert, S. Turner, The flow field downstream of a hydraulic jump, Journal of Fluid Mechanics 287 (1995) 299–316.
[11] S. Kucukali, H. Chanson, Turbulence measurements in hydraulic jumps with partially-developed inflow conditions, Experimental Thermal and Fluid Science 33 (1) (2008) 41–53, doi:10.1016/j.expthermflusci.2008.06.012.
[12] J.A. Liggett, Fluid Mechanics, McGraw-Hill, New York, USA, 1994.
[13] P.A. Madsen, A Model for a Turbulent Bore. Ph.D. thesis, Tech. Univ. of Denmark, Inst. of Hydrodyamics and Hyd. Eng., Copenhager, Denmark, 1981, 149 p (also Series Paper No. 28, Tech. Univ. of Denmark, Inst. of Hydrodyamics and Hyd. Eng., Copenhager, Denmark, 149 p.).
[14] D. Mouaze, F. Murzyn, J.R. Chaplin, Free surface length scale estimation in hydraulic jumps, Journal of Fluids Engineering, Transactions of the ASME 127 (2005) 1191–1193.
[15] F. Murzyn, H. Chanson, Free-surface fluctuations in hydraulic jumps: experimental observations, Experimental Thermal and Fluid Science 33 (7) (2009) 1055–1064, doi:10.1016/j.expthermflusci.2009.06.003.
[16] F. Murzyn, D. Mouaze, J.R. Chaplin, Air–water interface dynamic and free surface features in hydraulic jumps, Journal of Hydraulic Research IAHR 45 (5) (2007) 679–685.